The Cryosphere Discuss., 8, 5433–5483, 2014
www.the-cryosphere-discuss.net/8/5433/2014/
doi:10.5194/tcd-8-5433-2014

The Cryosphere Discussions
Open Access

Improving semi-automated glacial mapping with a multi-method approach: areal changes in Central Asia

T. Smith[1], **B. Bookhagen**[1], **and F. Cannon**[2]

[1]Institute of Earth and Environmental Science, Universität Potsdam, Potsdam, Germany
[2]Geography Department, University of California, Santa Barbara, USA

Received: 31 July 2014 – Accepted: 25 September 2014 – Published: 17 October 2014

Correspondence to: T. Smith (tsmith@uni-potsdam.de)
and B. Bookhagen (bodo@geo.uni-potsdam.de)

Published by Copernicus Publications on behalf of the European Geosciences Union.

Abstract

Central Asia has been strongly impacted by climate change, and will continue to be impacted by diverse climate stressors in the coming decades. This study aims to decipher the impact of climate change on glaciers in the central Tien Shan Mountain Range, a large and understudied region located northeast from the Pamir Knot.

To address glacier characteristics over a wide swath of Central Asia, the authors designed and implemented a glacial mapping algorithm which delineates both clean glacial ice – methods which are well documented – and glacial debris tongues, which often require extensive manual digitization. This research improves upon methods developed to automatically delineate glacial areas using spectral, topographic, velocity, and spatial relationships. The authors found that the algorithm misclassifies between 2 and 10 % of glacial areas, as compared to a ~ 750 glacier control dataset.

After validating the algorithm against multiple manually digitized control datasets, the authors applied it to a study area encompassing eight Landsat scene footprints stretching from the central Pamir through the central Tien Shan. A statistically significant, though minor, gradient in glacier area loss was found, where glaciers in the west of the study area have shrunk less than those glaciers in the east. This gradient is explained by differences in regional climate, where extratropical cyclones propagating from the west weaken and disband under continued topographic influence, as well as differences in topography, where high-elevation glaciers are thermally insulated from some of the impacts of changing temperatures in the region.

1 Introduction

A combination of changing weather patterns and shrinking glaciers has begun to impact water resources in Central Asia. The rate, extent, and mechanisms of these changes are poorly quantified due to a lack of data and process understanding. Glaciers serve as important seasonal water reservoirs in much of the Tien Shan and

TCD
8, 5433–5483, 2014

Pamir Ranges by providing meltwater after periods of snowmelt and before major rains. Increased understanding of changes in these glaciers is essential for sustainable water management, and mitigating the impacts of climate change on populations in Central Asia.

Changes in glacier length have long been considered one of the best indications of climate change (i.e. Oerlemans, 2005), though more recent studies have also assessed glacial volume changes with the advent of new remote sensing techniques (e.g., Berthier et al., 2007; Aizen et al., 2007; Gardelle et al., 2012, 2013; Bolch et al., 2012; Kääb et al., 2012; IPCC, 2013). This study focuses on assessing glacial length fluctuations over a large spatial scale using publicly available remotely sensed data. Several attempts have been made to produce accurate and high-resolution glacial outlines, most notably the Global Land Ice Measurements from Space (GLIMS) project (Armstrong et al., 2005; Raup et al., 2007, 2014), and the recently produced supplemental GLIMS dataset known as the Randolph Glacial Inventory (RGI) V3.2 (Arendt et al., 2012; Pfeffer et al., 2014). A coherent, complete, and accurate global glacial database is important for several reasons, including monitoring global glacial changes driven by climate change, natural hazard detection and assessment, and assessment of the role of glaciers in natural and built environments, including glacial contributions to regional water budgets and hydrologic cycles (Racoviteanu et al., 2009). Precision in glacial outlines is of utmost importance for monitoring changes in glaciers, which may only change by 15–30 m yr^{-1} (~ 1–2 pixels of Landsat Enhanced Thematic Mapper (ETM+) yr^{-1}). Thus, spatially accurate glacial outlines are imperative for precise glacial change detection (Paul et al., 2004, 2013).

Several methods have been developed to delineate clean glacial ice (i.e. Paul, 2002; Paul et al., 2002; Racoviteanu et al., 2008a, b; Hanshaw and Bookhagen, 2014), relying primarily on spectral data available from satellites such as Landsat and Advanced Spaceborne Thermal Emission and Reflection Radiometer (ASTER). Several researchers have also investigated the application of remote sensing datasets to snow cover determination, through both assessments of sub-pixel snow-covered area and

TCD
8, 5433–5483, 2014

grain size (i.e. Dozier, 1989; Painter et al., 2003, 2009; Dozier and Painter, 2004). Analysis of seasonal snow cover throughout the study area is based on these studies; snow cover is an important climatic indicator used in assessing trends in snow-covered area across Central Asia.

Although significant progress has been made towards automated glacial outline retrieval using satellite imagery, these methods struggle to accurately map debris-covered glaciers or other glaciers with irregular spectral profiles (Paul et al., 2004; Bolch et al., 2007; Racoviteanu et al., 2008b; Scherler et al., 2011a). Much of this difficulty stems from the similarities in spectral profiles of debris located on top of a glacial tongue and the surrounding hillslopes from which the debris is sourced. The majority of studies examining debris-covered glaciers employ extensive manual digitization in a Geographic Information System (GIS), which is very time consuming, and can introduce significant user-generated errors (Paul et al., 2013; Pfeffer et al., 2014; Raup et al., 2014). Building on the multi-spectral, topographic, and spatially-weighted methods developed by Paul et al. (2004), the authors present a refined rules-based classification based on spectral, topographic, land-cover, velocity, and spatial relationships between glacial areas and the surrounding environment.

Using a suite of 62 Landsat Thematic Mapper (TM), Enhanced Thematic Mapper+ (ETM+) and Optical Land Imager (OLI) images across a spatially and topographically diverse set of study sites comprising eight Landsat footprints (path/row combinations: 144/30, 145/30, 147/31, 148/31, 149/31, 151/33, 152/32, 153/33) along a profile from the central Pamir to the central and central-eastern Tien Shan (Fig. 1), the authors (1) pre-process the imagery (georeference and co-register), (2) apply the algorithm based on spectral, topographic, velocity, and spatial information, (3) analyze range-wide trends in glacial character, and (4) link spatially heterogeneous glacial area loss to climate factors. We address the hypothesis that spatially heterogeneous glacial shrinkage in our study region is driven by precipitation gradients.

TCD
8, 5433–5483, 2014

2 Study area and data sources

2.1 Study area

The wintertime climate of the study area is controlled by both the Winter Westerly Disturbances (WWDs) and the Siberian High, which dominate regional circulation and create strong precipitation gradients throughout the Tien Shan Range, which extends from Uzbekistan in the west through China in the east (Fig. 1) (Lioubimtseva and Henebry, 2009; Narama et al., 2010; Bolch et al., 2011; Sorg et al., 2012; Cannon et al., 2014). The western edges of the study region tend to receive more winter precipitation in the form of snow, with precipitation concentrated in the spring and summer in the central and eastern reaches of the range (Narama et al., 2010).

Sorg et al. (2012) note that due to the interaction of the Siberian High – a semi-permanent thermal high-pressure system that extends from Siberia towards the Tien Shan – and more western continental atmospheric patterns such as WWDs, the study area has a distinct precipitation gradient with decreasing precipitation from the west to east. There is also a strong gradient between outer and inner reaches of the Tien Shan, as moisture is precipitated on the windward (outer) side of topography, moving eastwards from the Pamirs (Sorg et al., 2012).

Several smaller-scale studies have examined glacial changes in the Tien Shan (e.g., Aizen et al., 1997, 2006; Narama et al., 2006, 2010; Shangguan et al., 2009; Osmonov et al., 2013). Narama et al. (2010) found that for the period of 1970–2010, glacial area decreased between 9 and 19 %, depending on the subregion of the Tien Shan analyzed. Glacial loss was then seen to accelerate between 2000 and 2007, except in a few cases in the southeastern reaches of the Tien Shan (Narama et al., 2010). This agrees generally with work by Narama et al. (2006), who noted that total glaciated area in the northern and central Tien Shan had shrunk by 14.2 % between the 1860s and 2003, with the bulk of shrinking occurring between 1977 and 2003. Several larger scale studies (e.g., Kääb et al., 2012; Bolch et al., 2012; IPCC, 2013) have looked at glacial changes over large scales, but lack sufficient spatial detail to fully constrain the rates

TCD
8, 5433–5483, 2014

and mechanisms of glacial change in the region, as well as potential linkages between differences in area loss rates and local or regional climate.

2.2 Data sources

Our glacial mapping algorithm is based on several datasets. The Landsat 5 (TM), 7 (ETM+), and 8 (OLI) platforms were chosen as the primary spectral data sources, as they provide spatially and temporally extensive coverage of the study area (Table 1). ASTER can also be used as a source of spectral information, but here the authors chose to focus on the larger footprint and longer timeseries available through the Landsat archive. In addition to spectral data, the 2000 Shuttle Radar Topography Mission (SRTM) Digital Elevation Model (DEM) (~ 90 m) was leveraged to provide elevation, slope, and hillshade information (Farr and Kobrick, 2000). The SRTM data and its derivatives were downsampled to 30 m to match the resolution of the Landsat images using bilinear resampling. The USGS Hydrosheds river network (15 s resolution) was also used as an input dataset (Lehner et al., 2008).

Several climatic datasets were analyzed to provide context to the analysis of glacial changes in the study area. Daily gridded Advanced Microwave Scanning Radiometer (AMSR-E) data (0.25° × 0.25° resolution) was used to estimate the snow–water equivalent (SWE) stored throughout the study area on a yearly basis (2002–2011) (Tedesco et al., 2004). The AMSR-E satellite measures microwave brightness temperatures at different frequencies to analyze snow depth, although the algorithm assumes a homogeneous snowpack with constant grain size (Tedesco and Narvekar, 2010). SWE measurements are further complicated by changing snow densities, which are not well represented in the AMSR-E dataset, because it converts estimated snow depth to a water equivalent. Despite these caveats, the AMSR-E SWE measurements remain the best estimates of the water stored in snowpack throughout much of the world, and especially in remote and understudied areas such as the Tien Shan.

Tropical Rainfall Measurement Mission (TRMM) data (products 3B42 and 3B43 V7) with a spatial resolution of 0.25° × 0.25°, aggregated into monthly and yearly means

TCD
8, 5433–5483, 2014

(1998–2014), were used to analyze precipitation across the range (Huffman et al., 2010; Bookhagen, 2010; Bookhagen and Burbank, 2010; Duan and Bastiaanssen, 2013). The precipitation radar (PR) onboard TRMM primarily senses rainfall, as liquid water is easier to detect by radar, although the TRMM datasets used in this study also contain information from several other datasets (e.g., AMSR-E precipitation estimates, infrared (IR) imagery from several satellites including Geosynchronous Operational Environmental Satellites (GOES), Multifunctional Transport Satellite (MTSat), and Meteorological Satellite (Meteosat), Advanced Microwave Sounding Unit (AMSU-B), as well as Global Precipitation Climatology Centre (GPCC) ground-based rainfall measurements), which are merged during processing to improve precipitation estimates (Huffman and Bolvin, 2007).

Two Moderate Resolution Imaging Spectroradiometer (MODIS) products, MOD10C1 (snow covered area, SCA) and MOD11C1 (land surface temperature, LST) were used to analyze yearly average snowcover and atmospheric lapse rates respectively (Hall and Salomonson, 2006; Wan, 2008). MOD10C1 data between 2001 and 2014 were aggregated to seasonal timesteps at $0.05^{\circ} \times 0.05^{\circ}$ spatial resolution. MOD11C1 data was aggregated seasonally to calculate atmospheric lapse rates at $0.05^{\circ} \times 0.05^{\circ}$ spatial resolution using SRTM elevation data. Lapse rates were calculated using night time temperatures, which have been shown to be more consistent in alpine regions (Colombi et al., 2007). A recent study validated MODIS LST data in the region by comparing ground station data for western Tibet with generated LST products, finding generally good agreement across both day and night (Wang et al., 2007).

Daily Climate Forecast System Reanalysis (CFSR) data were obtained at $0.5^{\circ} \times 0.5^{\circ}$ spatial resolution over the time period 1979–2010 (Saha et al., 2010). The dataset was chosen on account of its model coupling, spatial resolution, and modern assimilation system. CFSR's horizontal resolution is the best available for resolving the study region's complex topography. The data were analyzed for precipitable water, vertically integrated moisture flux, and geopotential heights. Using these data, a basic climatology

TCD
8, 5433–5483, 2014

was developed for the study region to inform analysis of changes in glacier character throughout the range.

It is important to note the lack of climate station data in the study region, especially at high elevations (Schöne et al., 2013). Previous studies in the region (e.g, Osmonov et al., 2013) have used low elevation stations (~ 3600 m), which are well below the median elevation of most glaciers in the study region. Due to the extent of our study region, the authors have chosen to rely on large-scale satellite data for climate and atmospheric analysis in the place of ground station data.

The RGI V3.2 dataset is comprised of ~ 198 000 glaciers with an estimated extent of 726 800 ± 34 000 km^2 (Pfeffer et al., 2014). This dataset was derived from previous glacier inventories, as well as satellite imagery over the period of 1999–2010, and provides complete global coverage, excepting ice sheets. This dataset was intended for wide-scale analysis, and has been successfully used to improve estimates of global glacial changes, and their contribution to sea-level rise. In our study, the dataset is used as a comparison dataset against which to analyze algorithm-derived glacial outlines. It is important to note, however, that the RGI was not designed for detailed glacial comparisons, and it is included in this study not because of its accuracy with specific glaciers, but rather because of its wide use in glacial analysis and its position as the most complete glacier inventory of the study area.

3 Methods

3.1 Data preparation

For accurate glacial delineation, the authors used primarily those Landsat images that were free of new snow, and had less than 10 % cloud cover. The presence of fresh snow in images tends to overclassify glacial areas and classify non-permanent snow as glaciers. Additionally, cloud cover tends to confuse the algorithm, and render

TCD
8, 5433–5483, 2014

glacial outlines that overlap with cloud cover unreliable (Paul et al., 2004; Hanshaw and Bookhagen, 2014).

After selecting a series of Landsat images, the authors co-registered each image to a "master" image specific to each Landsat path/row combination, using the Automated Registration and Orthorectification Package (AROP) (Gao et al., 2009). Master images are denoted in Table 1 with an asterisk. This ensures that glacier outlines are properly matched, and that any timeseries of glacial change is consistent in space. Once the data were georeferenced and registered, a series of scripts written in Python and Matlab performed the glacier classification (flow diagram shown in Fig. 2, source code available at: http://www.github.com/ttsmith89/GlacierExtraction/). The algorithm uses Landsat imagery, a hydrologically corrected DEM, a velocity surface derived from image cross-correlation, and the Hydrosheds 15 s river network (buffered by 200 m and converted to a raster) as the primary inputs. A script prepares these datasets for processing by resampling and reprojecting each dataset to the same spatial extent, resolution (30 m to match the Landsat data), and projection. It further generates slope and hillshade images from the DEM, and rectifies additional input datasets described below. Although the current algorithm is based on proprietary software, the authors will continue to update the code with the goal of using only open source tools and libraries in the future.

3.2 Lake delineation

Glacial debris tongues tend to host supra-glacial lakes, particularly during the summer months when snow cover is lowest (Quincey et al., 2007; Gardelle et al., 2011). These lakes can be used as seed points for distance-weighting mechanisms to more accurately delineate glacial debris tongues. Lakes are delineated using the Normalized Difference Water Index (NDWI) (Gao, 1996), after which misclassified areas are removed by masking out high slopes and shadowed areas (Huggel et al., 2002; Worni et al., 2013; Nie et al., 2013; Hanshaw and Bookhagen, 2014). To increase the modularity of the algorithm, the authors did not rely on a fixed NDWI value across all datasets, but

TCD
8, 5433–5483, 2014

instead used a manually generated set of index lakes that exhibit the spectral properties desired. This small manual step greatly increases the number of correctly classified lakes by providing scene-specific NDWI thresholds for each processed image.

3.3 Glacier delineation

3.3.1 Spectral delineation

Calculations are performed on rasterized versions of each input dataset, which have been standardized to the same matrix size. The first step in the classification process leverages Landsat Bands 1, 3, and 5. For Landsat 8 OLI images, a slightly different set of bands is used to conform to the modified spectral range of sensors on Landsat 8. For simplicity, bands referenced in this publication refer to Landsat 7 ETM+ spectral ranges. The ratio of TM3/TM5 (value ≥ 2), with additional spectral information from TM1 (value > 250) has long been established as an effective means of delineating glacier areas (e.g., Hall et al., 1987; Hanshaw and Bookhagen, 2014), but is not effective in delineating debris-covered glacier areas (Fig. 3). Shadowed areas derived from a SRTM-generated hillshade specific to the date and time of each Landsat image, as well as lake areas derived in the previous lake processing step, are then removed from this initial spectral classification (Huggel et al., 2002; Hanshaw and Bookhagen, 2014). The end result of this step is the spectrally-derived glacier outlines, which are later integrated back into the workflow before statistical filtering.

3.3.2 Topographic filtering

Building on the work of Paul et al. (2004), low slope areas (between 1 and 24°) are isolated as areas where debris-covered glaciers are likely to exist. As glacial surfaces tend to be rougher than the surrounding areas, a standard deviation filter (3×3 kernel size) is also applied to the slope and used to mask out areas of low slope variability. Low elevation areas (defined on a scene-by-scene basis) are then masked out to decrease

TCD
8, 5433–5483, 2014

processing time. These thresholding steps are performed independently of the previous, spectrally delineated, glacier outlines. In essence, this step identifies areas where there is the potential for a debris-covered glacier to exist. Additional thresholding is then performed on this "potential debris area" subset to identify debris-covered glacier areas.

The Correlation Image Analysis Software (CIAS) tool (Kääb, 2002), which uses a method of statistical image cross-correlation, is used to derive glacial velocities from Landsat Band 8 panchromatic images. This method functions by tracking individual pixels across space and time, and provides a velocity surface at the same resolution as the input datasets (15 m). The velocity surface is then upsampled using bilinear resampling to provide a consistent velocity estimate across the entire Landsat scene. The authors then standardized the velocity measurements to $m\,yr^{-1}$ using the capture dates of the two Landsat images. It is important to note that cloud-free and snow-free images are essential for this step, as the presence of snow or cloud cover can disrupt the correlation process, resulting in anomalous velocity measurements.

The authors only used one multi-year velocity measurement for each path/row combination to derive general areas of movement/stability for glacial classification, as using stepped velocity measurements over smaller time increments did not show a noticeable improvement in glacial classification. These velocities ranged generally from 4–$30\,m\,yr^{-1}$ across the different scenes, and were chosen based on both manual inspection of the velocity surfaces, and their impact on glacial classification on a test dataset. Furthermore, a method of frequential cross-correlation using the co-registration of optically sensed images and correlation (COSI-Corr) tool (Leprince et al., 2007; Scherler et al., 2011b) was tested and did not show any appreciable improvement in velocity measurements (Heid and Kääb, 2012).

Two additional topographic indices were tested here, although neither provided significant improvement to the algorithm: spatial Fast Fourier Transforms (FFTs), also known as 2-D FFTs, and ASTER surface roughness measurements. The authors attempted to derive frequential information from several Landsat and ASTER bands, with

TCD
8, 5433–5483, 2014

limited success. Some glaciers exhibited a unique frequency signature when analyzed using spatial FFTs, although these were not consistent across multiple debris-covered glaciers with differing surface characteristics. Additionally, the FFT approach was tested against a principal component analysis (PCA) image derived from all Landsat bands, without significant improvement to the algorithm.

The authors also attempted to integrate surface roughness measurements using the ASTER satellite, which contains both forward looking (3N – nadir) and backwards looking (3B – backwards) images, primarily intended for the generation of stereoscopic DEMs. The difference in imaging angle provides the opportunity to examine surface roughness by examining changes in shadowed areas (Mushkin et al., 2006; Mushkin and Gillespie, 2011). The authors found that there are slight surface roughness differences between glaciated and non-glaciated areas on some debris tongues, but that these differences are not significant enough to use as a thresholding metric. Furthermore, the nature of the steep topography limits the efficacy of this method, as valleys that lie parallel the satellite flight path and those that lie perpendicular to the flight path show different results. Thus, the algorithm relies on the velocity and slope thresholds to characterize the topography of the glacial areas.

The velocity step is most important for removing hard-to-classify pixels along the edges of glaciers, and wet sands in riverbeds. These regions are often spectrally indistinguishable from debris tongues, but have very different velocity profiles. It is important to note, however, that this step also removes some glacial area, as not all parts of a glacier are moving at the same speed. This can result in small holes in the delineated glaciers, which the algorithm attempts to rectify using statistical filtering.

3.3.3 Spatial weighting

After topographic and velocity filtering, a set of spatially weighted filters was constructed. The first filtering step uses the hydrosheds river network to remove "potential debris areas", which are distant from the center of a given glacial valley. As glaciers occur along the flowlines of rivers, and the hydrosheds river network generally delineates

TCD
8, 5433–5483, 2014

flowlines all the way to the peaks of mountains, the river network provides an ideal set of seed points with which to remove misclassified pixels. A second distance weighting is then performed using both the supra-glacial lakes detected during the lake delineation step, and the spectrally delineated glaciers. As debris tongues must occur in proximity to one or more of: (1) glacier areas, (2) the centerlines of valleys, or (3) supra-glacial lakes, this step is effective at removing overclassified areas. At this step, it is also possible to add manual seed points, which may be necessary for some longer debris tongues. The authors note that these are optional, and the majority of glaciers do not need the addition of manual seed points. However, for certain glaciers that do not have many lakes, or do not have lakes large enough to be delineated by Landsat, adding a few manual control points greatly increases the efficacy of the algorithm.

The spatial weighting step is essential for removing pixels that are spatially distant from any glacier or lake area. In many cases, large numbers of river pixels, and in some cases dry sand pixels, have similar spectral and topographic profiles to debris covered glaciers. This step effectively removes the majority of pixels outside the general glaciated area(s) of a Landsat scene.

3.3.4 Masking and filtering

Once the spatial weighting steps are completed, the glacial outlines are generally accurate. Additional filtering and smoothing steps help to remove some misclassified pixels due to errors in the SRTM DEM, high velocities in non-glacier areas, and areas with similar spectral profiles to glaciers. An NDWI mask is applied to remove dry areas, as glaciers uniformly exhibit a moisture signal that is detectable with NDWI. A Normalized Difference Vegetation Index (NDVI) mask is also applied, as glaciers in the study region rarely have noticeable vegetation. The authors note that all of the threshold parameters are set on the basis of Landsat scene path/row combinations to account for the slightly different topographic, velocity, and landcover settings of spatially diverse Landsat scenes. In general, one set of parameters is sufficient to characterize glaciers within multiple Landsat scenes with the same spatial extent (path/row combination)

TCD
8, 5433–5483, 2014

throughout time. However, scenes with extensive cloud cover or snow cover sometimes need separate thresholds to account for the differences in spectral signatures between cloud-free and cloud-covered images.

A set of median filters are then applied, as well as a set of statistical filters designed to remove isolated pixels (3×3 median filter, applied twice, as well as 5×5 median filter, applied after image opening), bridge gaps between isolated glacial areas (image bridging), and fill holes in large contiguous areas (image opening, applied twice). After these filters have been applied, the resulting glacial outlines are post-processed in order to add metadata to each glacier, remove very small glacial areas ($\sim$ 10–20 px or less), and export the results in vector format.

This step is essential for filling holes and reconnecting separated glacier areas. As the filtering methods used are based on a fixed set of threshold values, there are often glacier pixels that are removed. For example, some pixels along the edge of a debris tongue may be moving slower than the provided velocity threshold, and are thus removed. This problem is somewhat, but not completely, remedied by the statistical filtering (Fig. 4).

3.4 Creation of manual control datasets

Two manual control datasets encompassing $\sim$ 750 glaciers ($\sim$ 3000 km^2) each were created to test the efficacy of the glacial mapping algorithm. The authors note that although the manual datasets here are considered "perfect", there is inherent error in any manual digitization in a GIS (e.g., Paul et al., 2013). Due to the lack of ground truth information, the authors have estimated the overall uncertainty of the manual dataset to be 2 % (Paul et al., 2002, 2013).

Before any comparisons between glaciers can be performed, contiguous glacial areas – both due to snowcover and to ice caps – must be split into component parts. A set of manually edited watershed boundaries, derived from both the SRTM DEM and compared to the glacial delineations provided by the RGI, were used to split both the manual and algorithm datasets into individual glacial areas for analysis. In this manner,

TCD
8, 5433–5483, 2014

the diverse datasets and classified glacial areas can be split into the same subset areas for statistical comparison.

4 Results

4.1 Statistical analysis of algorithm errors

A subset of 138 glaciers from the two manual control datasets of varying size and topographic setting was chosen for more detailed analysis. The unedited, algorithm-generated, glacial outlines were compared against three separate datasets: (1) the RGI V3.2 (Arendt et al., 2012), which is considered due to its position as the most complete and accurate global glacial database; (2) spectral outlines, which only classify the glacial areas via commonly used spectral subsetting (using TM1, TM3, and TM5); and (3) a manual control dataset, which was hand-digitized by the authors from Landsat imagery. Figure 5 shows the bulk elevation distributions across 138 glaciers for each dataset in 10 m elevation bins. An additional set of figures showing the effects of each step of the algorithm on glacier classification are available in the Supplement.

From these distributions, it is apparent that the RGI universally overclassifies glacial areas, and that using only a spectral classification tends to overclassify high-elevation areas and underclassify low-elevation areas. It is important to note that the RGI was not intended for direct glacial comparisons as it is used here. The authors use it here as the best publicly available glacial database against which to compare our results over a large area. There is some apparent bias in the authors' algorithm towards low-elevation areas, which represent the debris-covered portions of glaciers and are the most difficult areas to classify. To illustrate the difference between the manual control dataset and each of the comparison datasets, the elevation distributions were differenced in Fig. 6.

In general, the same patterns appear in Fig. 6 as in Fig. 5: that is, the spectral-only method overclassifies in high elevations and underclassifies in low elevations, and the

TCD
8, 5433–5483, 2014

algorithm-derived dataset underclassifies low-elevation areas. However, at any given elevation slice, the algorithm-derived data were off by less than 0.5 % from the area of the manual control dataset, and are generally well matched at elevations above 4000 m. The underclassification at the 3500–4000 m class can be attributed to hard-to-classify side glaciers, or tributary glaciers. Many of these glaciers are located in shaded or otherwise topographically distinct valleys, which can result in underclassification of connected glacial areas, although an analysis of shadowed-area mismatches between manual and algorithm datasets indicates that shadowed areas are responsible for only very small misclassifications ($\sim 4 \times 10^{-8}$ km^2, $\sim$5–10 px per elevation slice). Over the span of a single Landsat scene, or even over most individual watersheds within a Landsat scene, the elevation distributions of the manual and algorithm datasets are virtually indistinguishable (ks-test at the 99 % confidence interval passes).

In order to examine persistent bias throughout the algorithm classification, under- and over-classified areas were examined. To determine areas of overclassification (underclassification), the manually (algorithm) generated dataset was subtracted from the algorithm (manual) dataset, leaving only pixels that were overclassified (underclassified). Figure 7 shows the elevation distributions of under- and over-classified areas. The algorithm tends to consistently overclassify areas above 4500 m, and underclassify areas under 4500 m, though much of this misclassification occurs at similar elevation slices, and thus in bulk the mismatch between the manual and algorithm derived datasets is minimal. The total misclassification of algorithm-derived outlines against the two control datasets is 2 and 10 % respectively, which represents a significant improvement from a pure spectral delineation approach. The authors would like to emphasize that these offsets refer to the unedited algorithm-derived outlines, before any manual corrections have been applied.

Finally, a set of topographic indices was examined to determine if there was a misclassification bias towards a certain elevation, size, aspect, or slope setting (Fig. 8). The results of this analysis are that none of the topographic indices show a strong trend across the analyzed glaciers, although there is a slight bias towards underclassifying

TCD
8, 5433–5483, 2014

lower-elevation areas vs higher-elevation areas, and underclassifying lower-slope areas. These are known errors associated with the difficulty of classifying glacial tongues, particularly those with heavy debris cover. However, on average, the mismatch between the algorithm and manual control datasets is minimal regardless of topographic setting (between 2–10 %). It is important to note that the algorithm datasets used in the statistical analysis were not manually edited, and are the direct output of the authors' algorithm.

4.2 Comparison to a random sampling of glacial areas

In order to examine sampling bias in our analysis, the researchers used 465 GLIMS glacier identification numbers (centroids, point features) that overlapped with the manual control datasets. A random subset of 100 of these points was chosen for this analysis. As can be seen in Fig. 9, similar patterns emerge between the randomly sampled glaciers and the sampling used in other sections of this manuscript. There is evidence of increased noise in the random sample, as some glaciers that were avoided by the researchers due to closeness to wet sand or other hard-to-classify areas were chosen during the random sampling. However, in general, the relationship between the algorithm and the manual datasets remains significant (ks-test passes at 99 % confidence interval).

5 Discussion

Using the newly developed glacier delineation algorithm, the authors analyzed shrinkage rates of glaciers from the central Pamir through the most heavily glaciated region of the Tien Shan (Fig. 1). Minimal manual inspection and rectification was performed on glaciers used in the areal-change analyses, to ensure that algorithm errors were not propagated into the discussion of glacier change. A dataset of 313 glaciers was used to examine shrinkage trends across the study area.

TCD
8, 5433–5483, 2014

5.1 Area loss in selected glaciers

Two example glaciers were chosen to display specific area changes (Figs. 10 and 11). Both, glaciers have lost area over the period 1998–2014. Including additional data sources such as Corona, Landsat Multispectral Scanner (MSS), ASTER, and non-cloud-free Landsat TM, ETM+ and OLI images was outside of the scope of this study.

The authors would like to note that the primary use of the algorithm is in assessing trends at a larger spatial scale, using dozens of glaciers, and not in assessing trends within individual glaciers. Due to the difficulties inherent in dividing one glacier area from another, particularly at high-elevation areas where snowcover often connects multiple glaciers, area changes on a glacier-by-glacier basis are associated with larger uncertainties and require significant manual work to separate combined glacial area into individual glaciers. Furthermore, over- and under-classified areas, which tend to even out over a large spatial scale, can present problems at the scale of individual glaciers, especially in complex terrain or in the case of debris-covered glaciers. An effort was made to choose glaciers that are somewhat isolated to demonstrate areal changes at a small scale, using both the algorithm and some manual corrections at the glacial tongue. The algorithm is most useful when glacier area changes are assessed at a watershed, drainage basin, or range-wide scale.

5.2 Areal changes in glaciers in the study area

The total mapped glacier area across the eight Landsat scene footprints used in this study was approximately $9444.7 \pm 189\,km^2$ circa the year 2000, with $4376.75\,km^2$ manually inspected, edited, and used for statistical analysis. The bulk area loss rate across glaciers that were quality controlled was 3.9 % (total area loss of $172.24\,km^2$ over the period ~ 1999 to ~ 2014). The area loss rates across the study area vary widely and can change significantly within the confines of a single Landsat scene footprint. Furthermore, the diverse scene-capture times make establishing a single bulk loss rate

TCD
8, 5433–5483, 2014

for the whole study area difficult, and thus our 3.9 % shrinkage rate represents only an estimate of the total area loss in glaciers in the study area.

5.2.1 Relationship with previous studies

Several smaller scale studies have examined glaciers and glaciated areas that overlap with our study area. Using both raw and minimally corrected algorithm-derived glacier outlines, the authors have compared our area change rates for selected areas with those previously published in the literature. These values are presented in Table 2. The authors note that the shrinkage rates established in previous studies (with the exception of Osmonov et al., 2013) do not generally overlap our data in time and are thus difficult to compare. However, the area loss rates established in this study are comparable to those published in the literature, albeit with a slight increase in melt rates over the last decade, as noted previously by Aizen et al. (2006) and Narama et al. (2010).

5.2.2 Area loss rate gradient across the study area

Figure 12 illustrates the relationship between geographic location, from west to east, and areal changes across the study area. Although noise in the data is evident, all of the data were generated using the same methodology, and are thus comparable. The gradient of the fitted line is 7×10^{-4} km^2 yr^{-1} m^{-1} per decimal degree; a t test performed on the data shows that the trend is significant at the 95 % confidence level. The one caveat to this is that the authors have noted that not all Landsat scenes perform equally; scenes with excess snow, cloud cover, shadows, or other strong spectral signatures may lead to the misclassification of some glacial areas. The authors have also noted that OLI images generally perform better than TM or ETM+ images, particularly in images with cloud and snow cover. However, this relationship has not been substantiated with thorough statistical analysis, and should not be considered definite. The authors posit that the increased pixel depth with the 12-bit dynamic range sensor on the OLI platform is responsible for the increased classification fidelity through

TCD
8, 5433–5483, 2014

decreased image saturation, but this relationship remains speculative. An effort was made to choose only the best suited images for this study; as can be seen from the statistical analysis presented above, the glacier outlines are generally accurate, particularly when considered in larger quantities. Any scenes with cloudcover used in this analysis have been visually inspected and manually corrected.

Regional bulk areal change rates do not necessarily represent an accurate accounting of glacial health – for example, high-elevation glaciers will generally change more slowly than low-elevation glaciers. This research has chosen to normalize the areal change rate data by the median elevation of each glacier (Hanshaw and Bookhagen, 2014). When the data are normalized by other indices, such as median slope and area, the relationship remains consistent, in that glaciers further to the east in the study area tend to have shrunk more than glaciers to the west, over the period ~1998–2014. When low-elevation glaciers (median elevation < 4000 m) are analyzed independently, areal change rates across the study area do not show a gradient, in that there is not significant variation from west to east. Glaciers above 4000 m, and in each individual elevation slice above that (broken into 250 m slices) show the same east/west gradient in areal change as the complete glacier dataset albeit, with varying longitudinal trends.

The gradient in glacial area changes agrees well with work by Gardelle et al. (2013), who noted that the Pamir Range has experienced slightly positive mass balances over the period 2000–2011. Although this study is focused on areal changes as opposed to the mass balances examined by Gardelle et al. (2013), the authors propose a similar mechanism for the variability in glacial area change rates: spatial gradients in precipitation. To understand climatic forcing across the range, the authors have analyzed several climatic and topographic variables to determine the factors responsible for the variation in change rates across the study area.

TCD
8, 5433–5483, 2014

5.3 Climatic influences

To analyze the impacts of climatic gradients across the study area on glacial behavior, the authors created a swath profile from the central Pamir through the central Tien Shan.

Figure 13a and b shows the general topography across the range from the Pamir Knot towards the eastern end of the Tien Shan. The highest elevation areas host the most glaciers, most notably the Pamirs on the west of the swath profile ($\sim 73^{\circ}$ E) and the area surrounding the Inylchek glacier $\sim 80^{\circ}$ E. Both SWE and precipitation in general are fairly low ($< 200\,\mathrm{mm\,yr^{-1}}$) throughout the range. Figure 13c shows precipitation and snow cover throughout the study area, as well as seasonal precipitation percentages. Winter (November–April) precipitation is dominant up until the eastern edge of the Pamirs, where summer (May–October) precipitation becomes dominant. As glacial response to summer and winter precipitation regimes is different (e.g., Narama et al., 2010), the split between the winter and summer growth regions could also explain some of the east-west variability in glacier area loss. This theory is also supported by the lack of east-west area loss gradient in low-elevation glaciers (< 4000 m), which are most strongly influenced by increasing temperatures in the region. Glaciers above this zone, which have also experienced shrinkage, receive relatively more snowfall, and are thus more sensitive to regional weather patterns' influence on precipitation.

The atmospheric lapse rates (Fig. 13d) illustrate generally cold temperatures year round in the Pamirs, and generally higher summer temperatures than winter temperatures throughout the remainder of the study area. Lapse rates are defined here as the change in atmospheric temperature (in this case, night-time land surface temperature, MODIS product MOD11C) over change in elevation, which gives a temperature gradient across the mountain range. The strongly negative lapse rates in the west indicate colder mountain peaks, which have a strong correlation with larger glacial areas. As lapse rates become less strongly negative towards the east, peaks become slightly warmer, and less glaciated overall. The glaciers to the east are also more likely to be

TCD
8, 5433–5483, 2014

impacted by warming temperatures, as they are situated in generally warmer areas to begin with.

There is a distinct precipitation gradient between the external watersheds and the internal watershed, which drains towards the Taklamakan Desert (generalized into internal and external components as a black line in Fig. 13a). The inner basin receives less rainfall, and has less snow covered area. Lapse rates are similar in the two regions, primarily due to generally cold temperatures year round. Unfortunately, TRMM 3B43 (or 3B42) data did not allow the authors to effectively measure snowfall (Palazzi et al., 2013), which is a key component in glacier area changes, and there is insufficient data to draw conclusions on whether or not the drainage divide influences glacier area change rates. It is unlikely that the north-south divide is as strong of a control on glacial areas in the region as the east-west gradient.

5.4 Atmospheric setting

We have identified an east to west gradient in glacier area change rates, but it is not clear what factors have driven the variable changes over the past ~16 yrs. To assess the influence of climate in this region, the authors have focused on atmospheric circulation and precipitation to create lag-composites detailing the impacts of wintertime extra-tropical cyclones along the Pamir and Tien Shan Ranges.

The WWDs are most active between January and March (Lang and Barros, 2004), and are responsible for the bulk of winter precipitation in HMA (Lioubimtseva and Henebry, 2009; Bookhagen and Burbank, 2010). Figure 14 indicates the propagation of an upper-level trough, which is a characteristic feature of WWDs, two days before through two days after 95th percentile precipitation (TRMM 3B42) events in the Pamirs (Fig. 14, left) and Tien Shan (Fig. 14, right). In both cases, the extratropical cyclone associated with this trough advects moisture from the Mediterranean, Caspian and Arabian Seas toward High Asia. Precipitable water over continental Asia is generally low due to extremely cold temperatures, thus this southwesterly moisture transport is a necessary element for dynamically driven orographic precipitation.

TCD
8, 5433–5483, 2014

In general, WWDs first encounter extreme topography in the Pamir and Hindu-Kush Regions, at the western extent of High Asia (Cannon et al., 2014). Their continued propagation is dependent on the angle of approach and upper-level steering, which may be determined by the position of the subtropical jet. This can result in systems either being topographically blocked or continuing to the north or south of the Tibetan Plateau. As a result, the Pamirs are open to a wider angle of WWD than the Tien Shan and thus experience more frequent extratropical cyclones with stronger dynamical forcing and higher moisture content than the downwind Tien Shan.

Figure 14, left, indicates that based on composites of 87 heavy precipitation events (95th percentile), WWDs encountering the Pamir Mountains generally do not produce heavy precipitation in the Tien Shan. Contrastingly, 95th percentile precipitation events in the Tien Shan are delivered by WWD that first encounter the Pamirs and deposit large amounts of precipitation, thus losing a significant amount of moisture before arriving in the Tien Shan (Fig. 14 right, day −1). This illustrates the differences in precipitation amounts between the Pamirs and Tien Shan, elicited by the average propagation of extratropical cyclones and orographic forcing. More consistent WWD influence and higher precipitation accumulation in the Pamirs during winter months may be sufficient to offset the effect of temperature changes with respect to glacial shrinkage. Contrastingly, the Tien Shan appears to be a more climatologically "fragile" region, and its glaciers may be relatively more vulnerable to slight changes in temperature as well as WWD. More generally, we suspect that the west to east gradient in WWD-produced precipitation creates a gradient in the tolerance of glaciers to temperature change due to the buffering influence of frequent snowfall events in regions of high WWD activity.

Both the Pamirs and the Tien Shan receive precipitation in the summer months due to the weakening of the Siberian High and northward migration of the subtropical jet, combined with increased atmospheric moisture content as a result of increased land-surface temperatures over Eurasia (Aizen et al., 1997; Sorg et al., 2012). Precipitation during the summer is less dependent on dynamical forcing of extratropical cyclones. During this time, the general state of the atmosphere is less thermodynamically stable

TCD
8, 5433–5483, 2014

and thus only weak forcing is required to drive precipitation in the mountains. In addition, the Tien Shan receives a higher proportion of its annual precipitation in the summer and is less affected by the Pamirs, which do not interfere with regional circulation to the same extent as in the winter, given the more northwesterly atmospheric flow (Mölg et al., 2012). Snowfall in the summer does contribute to glacial processes, although it is generally restricted to higher elevations, while at low elevations, precipitation falls as rain (Bolch, 2007). Given our study region's proximity to the Himalaya, it is worth mentioning that the Indian Summer Monsoon does not contribute to summer precipitation in the Tien Shan (Bookhagen and Burbank, 2010).

Recent work has identified that both the number of WWDs, and the amount of snowfall they generate, are likely to increase through the 21st century (Ridley et al., 2013; Palazzi et al., 2013). Although their analyses focused on the Karakorum, changes in WWDs may also impact the Tien Shan. Furthermore, Cannon et al. (2014) note that the wintertime subtropical jet shifted northward over the period 1979–2010, which altered the propagation of WWDs, increasingly favoring synoptic variability in the Pamirs and Tien Shan. This may have reduced glacial area loss by enhancing WWD activity during this time period, though it is difficult to qualify its affect given the issues with measuring precipitation as well as the numerous factors that must be taken into account when evaluating glacial processes.

5.5 Discussion of algorithm use cases and caveats

The glacier outlines provided by the algorithm are a useful first pass analysis of glacial area. It is often more efficient to digitize only misclassified areas, as opposed to digitizing entire glacier areas by hand (Paul et al., 2013). Paul et al. (2013) also note that for clean ice, automatically derived glacier outlines tend to be more accurate, and it is only in the more difficult debris-covered and shadowed areas that manual digitization becomes preferable. In the algorithm presented here, clean ice thresholding was implemented using TM1, TM3, and TM5, but as the algorithm primarily operates on "potential debris areas", as opposed to whole glaciers, different spectral classification

TCD
8, 5433–5483, 2014

schemes could be easily substituted for regions where other spectral measurements, such as the Normalized Difference Snow Index, perform best.

The algorithm moves a step further than spectral-only classification and attempts to classify glacier areas as accurately as possible, including debris-covered areas. As can be seen in Figs. 5 and 6, the algorithm performs very well over a large dataset (~750 glaciers). At the scale of watersheds, satellite-image footprints, or entire mountain ranges, this is an effective methodology which can be used to generate wide-area glacial statistics, as can be seen in Fig. 12. As the method can be easily modified to fit the topographic and glacial setting of any region, it is a powerful tool for analyzing glacier changes on large scales over the period of Landsat TM, ETM+ and OLI coverage. Lastly, as the algorithm performs well on debris-covered areas, it could be used in the place of simple spectral ratios, as it will often reduce the time required for manual digitization and correction, as compared to spectral-only methods.

Although the algorithm represents a step towards improved glacial classification, there are several important caveats to keep in mind. (1) Lack of data density and temporal range limits the efficacy of individual glacier analysis; the algorithm presented in this paper was not designed with individual glacier studies in mind, and in many cases, such as in mass balance studies, more accurate manual glacier outlines are necessary. Furthermore, (2) the algorithm relies heavily on the fidelity of the Landsat images provided, in that glacier outlines on images with cloud cover or snow cover are less likely to be well defined. This creates a data limitation, as many glaciated areas are subject to frequent snow and cloud cover, and thus have a limited number of potentially useful Landsat images for the purpose of this algorithm. The algorithm is also not well suited to Landsat MSS images, as the spectral and spatial resolution is generally too low for accurate classification. The final caveat of the algorithm is that (3) it relies on manual intervention to separate individual glaciers that are connected through snow cover, ice caps, or other overlapping classified areas. When examining individual glaciers, it is essential to first divide the algorithm-derived glacial outlines by watershed boundaries or other metrics.

TCD
8, 5433–5483, 2014

6 Conclusions

This study presents an enhanced glacial classification methodology based on the spectral, topographic, and spatial characteristics of glaciers. The authors have additionally applied the algorithm to analyze the character of glaciers across Central Asia from 1998–2014.

The authors' algorithm represents a step forward toward (semi-)automated glacial classification, in that it outperforms spectral-only algorithms in wide use in the glaciology and remote sensing communities. Although it does not completely solve the difficulties associated with debris-covered glaciers, it can effectively and rapidly characterize glaciers over a wide area. The first steps of this algorithm, which seek to characterize maximum possible glacier area, are lake delineation, spectral delineation, and topographic filtering. Following these steps, a set of velocity, spatial, and statistical filters are applied to accurately delineate glacier outlines.

Using this newly developed algorithm, the authors present evidence that glacial change rates across the Tien Shan show a west to east gradient. Although the difference in area loss rate is small, it has been shown to be statistically significant, and the authors can say with confidence that glaciers closer to the Pamirs (west) are shrinking less than those closer to the Altai (east). To explain this gradient, the authors analyzed climate and topographic data, which reveal a west to east trend in precipitation that matches the general trend in area loss rates. Extratropical cyclones propagating from the west first encounter topography in the western extent of our study region, including the Pamirs and western Tien Shan. Orographically driven precipitation associated with these disturbances contributes to high snowfall totals in these regions, while reducing the moisture available to the eastern Tien Shan as systems continue to propagate eastward. Consequently, annual snowfall totals are highest in the western regions, where westerly disturbances are most active. The eastern Tien Shan receives a higher proportion of its annual precipitation during the summer, and annual accumulation is well below the levels experienced in the west. This implies that the western

TCD
8, 5433–5483, 2014

regions receive both more precipitation overall, and that the majority of this precipitation in glaciated areas falls as snow. As a consequence of increasing temperatures in the region, summer-fed glaciers (towards the east of the study area) will be impacted by longer ablation seasons, shorter accumulation seasons, and shorter periods of high albedo (from fresh snow). All of these factors enhance glacial-area loss towards the east of the study area, while having weaker effects on the glaciers towards the west of the study area. In summation, the west-east glacier change gradient is driven by a combination of climate and topography.

The Supplement related to this article is available online at doi:10.5194/tcd-8-5433-2014-supplement.

Acknowledgements. This work was supported through the Earth Research Institute (UCSB) through a Natural Hazards Research Fellowship, as well as the NSF grant AGS-1116105.

References

Aizen, V. B., Aizen, E. M., Melack, J. M., and Dozier, J.: Climatic and hydrologic changes in the Tien Shan, central Asia, J. Climate, 10, 1393–1404, 1997. 5437, 5455

Aizen, V. B., Kuzmichenok, V. A., Surazakov, A. B., and Aizen, E. M.: Glacier changes in the central and northern Tien Shan during the last 140 years based on surface and remote-sensing data, Ann. Glaciol., 43, 202–213, 2006. 5437, 5451

Aizen, V., Aizen, E., and Kuzmichonok, V.: Glaciers and hydrological changes in the Tien Shan: simulation and prediction, Environ. Res. Lett., 2, 045019, doi:10.1088/1748-9326/2/4/045019, 2007. 5435

Arendt, A., Bolch, T., Cogley, J. G., Gardner, A., Hagen, J.-O., Hock, R., Kaser, G., Pfeffer, W. T., Moholdt, G., Paul, F., Radić, V., Andreassen, L., Bajracharya, S., Barrand, N., Beedle, M., Berthier, E., Bhambri, R., Bliss, A., Brown, I., Burgess, D., Burgess, E., Cawkwell, F., Chinn, T., Copland, L., Davies, B., De Angelis, H., Dolgova, E., Filbert, K., Forester, R. R.,

TCD
8, 5433–5483, 2014

Fountain, A., Frey, H., Giffen, B., Glasser, N., Gurney, S., Hagg, W., Hall, D., Haritashya, U. K., Hartmann, G., Helm, C., Herreid, S., Howat, I., Kapustin, G., Khromova, T., Kienholz, C., Köonig, M., Kohler, J., Kriegel, D., Kutuzov, S., Lavrentiev, I., Le Bris, R., Lund, J., Manley, W., Mayer, C., Miles, E., Li, X., Menounos, B., Mercer, A., Mölg, N., Mool, P., Nosenko, G., Negrete, A., Nuth, C., Pettersson, R., Racoviteanu, A., Ranzi, R., Rastner, P., Rau, F., Raup, B., Rich, J., Rott, H., Schneider, C., Seliverstov, Y., Sharp, M., Sigurðsson, O., Stokes, C., Wheate, R., Winsvold, S., Wolken, G., Wyatt, F., and Zheltyhina, N.: Randolph Glacier Inventory [v2.0]: A Dataset of Global Glacier Outlines. Global Land Ice Measurements from Space, Digital Media, Boulder Colorado, USA, 2012. 5435, 5447

Armstrong, R., Raup, B., Khalsa, S., Barry, R., Kargel, J., Helm, C., and Kieffer, H.: GLIMS Glacier Database, National Snow and Ice Data Center, Boulder, Colorado, USA, 2005. 5435

Berthier, E., Arnaud, Y., Kumar, R., Ahmad, S., Wagnon, P., and Chevallier, P.: Remote sensing estimates of glacier mass balances in the Himachal Pradesh (Western Himalaya, India), Remote Sens. Environ., 108, 327–338, 2007. 5435

Bolch, T.: Climate change and glacier retreat in northern Tien Shan (Kazakhstan/Kyrgyzstan) using remote sensing data, Global Planet. Change, 56, 1–12, 2007. 5456

Bolch, T., Buchroithner, M. F., Kunert, A., and Kamp, U.: Automated delineation of debris-covered glaciers based on ASTER data, in: Geoinformation in Europe, Proc. of 27th EARSel Symposium, 4–7 June 2007, Bozen, Italy, 403–410, 2007. 5436

Bolch, T., Peters, J., Yegorov, A., Pradhan, B., Buchroithner, M., and Blagoveshchensky, V.: Identification of potentially dangerous glacial lakes in the northern Tien Shan, Nat. Hazards, 59, 1691–1714, 2011. 5437

Bolch, T., Kulkarni, A., Kääb, A., Huggel, C., Paul, F., Cogley, J., Frey, H., Kargel, J., Fujita, K., Scheel, M., Bajracharya, S., and Stoffel, M.: The state and fate of Himalayan glaciers, Science, 336, 310–314, 2012. 5435, 5437

Bookhagen, B.: Appearance of extreme monsoonal rainfall events and their impact on erosion in the Himalaya, Geomatics, Nat. Hazard. Risk, 1, 37–50, 2010. 5439

Bookhagen, B. and Burbank, D. W.: Toward a complete Himalayan hydrological budget: spatiotemporal distribution of snowmelt and rainfall and their impact on river discharge, J. Geophys. Res.-Earth, 115, F03019, doi:10.1029/2009JF001426, 2010. 5439, 5454, 5456

Cannon, F., Carvalho, L., Jones, C., and Bookhagen, B.: Multi-annual variations in winter westerly disturbance activity affecting the Himalaya, Clim. Dynam., 1–15, doi:10.1007/s00382-014-2248-8, 2014. 5437, 5455, 5456

TCD
8, 5433–5483, 2014

Colombi, A., De Michele, C., Pepe, M., and Rampini, A.: Estimation of daily mean air temperature from MODIS LST in Alpine areas, EARSeL eProceedings, 6, 38–46, 2007. 5439
Dozier, J.: Spectral signature of alpine snow cover from the Landsat Thematic Mapper, Remote Sens. Environ., 28, 9–22, 1989. 5436
Dozier, J. and Painter, T. H.: Multispectral and hyperspectral remote sensing of alpine snow properties, Annu. Rev. Earth Pl. Sc., 32, 465–494, 2004. 5436
Duan, Z. and Bastiaanssen, W.: First results from Version 7 TRMM 3B43 precipitation product in combination with a new downscaling–calibration procedure, Remote Sens. Environ., 131, 1–13, 2013. 5439
Farr, T. G. and Kobrick, M.: Shuttle radar topography mission produces a wealth of data, EOS T. Am. Geophys. Un., 81, 583–585, 2000. 5438, 5470
Gao, B.-C.: NDWI – a normalized difference water index for remote sensing of vegetation liquid water from space, Remote Sens. Environ., 58, 257–266, 1996. 5441
Gao, F., Masek, J., and Wolfe, R. E.: Automated registration and orthorectification package for Landsat and Landsat-like data processing, J. Appl. Remote Sens., 3, 033515–033515, 2009. 5441
Gardelle, J., Arnaud, Y., and Berthier, E.: Contrasted evolution of glacial lakes along the Hindu Kush Himalaya mountain range between 1990 and 2009, Global Planet. Change, 75, 47–55, 2011. 5441
Gardelle, J., Berthier, E., and Arnaud, Y.: Slight mass gain of Karakoram glaciers in the early twenty-first century, Nat. Geosci., 5, 322–325, 2012. 5435
Gardelle, J., Berthier, E., Arnaud, Y., and Kääb, A.: Region-wide glacier mass balances over the Pamir-Karakoram-Himalaya during 1999–2011, The Cryosphere, 7, 1263–1286, doi:10.5194/tc-7-1263-2013, 2013. 5435, 5452
Hall, D., Ormsby, J., Bindschadler, R., and Siddalingaiah, H.: Characterization of snow and ice reflectance zones on glaciers using Landsat Thematic Mapper data, Ann. Glaciol., 9, 1–5, 1987. 5442
Hall, D. K., Riggs, G. A., and Salomonson, V. V.: MODIS/Terra Snow Cover Daily L3 Global 0.05 deg CMG V005, MOD10C1, National Snow and Ice Data Center, Boulder, Colorado, USA, 2006. 5439
Hanshaw, M. N. and Bookhagen, B.: Glacial areas, lake areas, and snow lines from 1975 to 2012: status of the Cordillera Vilcanota, including the Quelccaya Ice Cap, northern central

TCD
8, 5433–5483, 2014

Andes, Peru, The Cryosphere, 8, 359–376, doi:10.5194/tc-8-359-2014, 2014. 5435, 5441, 5442, 5452
Heid, T. and Kääb, A.: Evaluation of existing image matching methods for deriving glacier surface displacements globally from optical satellite imagery, Remote Sens. Environ., 118, 339–355, 2012. 5443
Huffman, G. J. and Bolvin, D. T.: TRMM and other data precipitation data set documentation, Laboratory for Atmospheres, NASA Goddard Space Flight Center and Science Systems and Applications, Inc. (WWW document), available at: ftp://meso-a.gsfc.nasa.gov/pub/trmmdocs/3B42_3B43_doc.pdf (last access: 23 March 2012), 2007. 5439
Huffman, G. J., Adler, R. F., Bolvin, D. T., and Nelkin, E. J.: The TRMM multi-satellite precipitation analysis (TMPA): quasi-global, multiyear, combined-sensor precipitation estimates at fine scales, J. Hydrometeorol., 8, 38–55, doi:10.1175/jhm560.1, 2010. 5439
Huggel, C., Kääb, A., Haeberli, W., Teysseire, P., and Paul, F.: Remote sensing based assessment of hazards from glacier lake outbursts: a case study in the Swiss Alps, Can. Geotech. J., 39, 316–330, 2002. 5441, 5442
IPCC: Climate Change 2013: The Physical Science Basis. Contribution of Working Group I to the Fifth Assessment Report of the Intergovernmental Panel on Climate Change, edited by: Stocker, T. F., Qin, D., Plattner, G.-K., Tignor, M., Allen, S. K., Boschung, J., Nauels, A., Xia, Y., Bex, V., and Midgley, P. M., Cambridge University Press, Cambridge, United Kingdom and New York, NY, SA, 1535 pp., 2013. 5435, 5437
Kääb, A.: Monitoring high-mountain terrain deformation from repeated air- and spaceborne optical data: examples using digital aerial imagery and ASTER data, ISPRS J. Photogramm., 57, 39–52, 2002. 5443
Kääb, A., Berthier, E., Nuth, C., Gardelle, J., and Arnaud, Y.: Contrasting patterns of early twenty-first-century glacier mass change in the Himalayas, Nature, 488, 495–498, 2012. 5435, 5437
Lang, T. J. and Barros, A. P.: Winter storms in the central Himalayas, J. Meteorol. Soc. Jpn., 82, 829–844, 2004. 5454
Lehner, B., Verdin, K., and Jarvis, A.: New global hydrography derived from spaceborne elevation data, EOS T. Am. Geophys. Un., 89, 93–94, 2008. 5438
Leprince, S., Ayoub, F., Klingert, Y., and Avouac, J.-P.: Co-registration of optically sensed images and correlation (COSI-Corr): an operational methodology for ground deformation mea-

TCD
8, 5433–5483, 2014

surements, in: Geoscience and Remote Sensing Symposium, 23–28 July 2007, Barcelona, IGARSS 2007, IEEE International, IEEE, 1943–1946, 2007. 5443
Lioubimtseva, E. and Henebry, G. M.: Climate and environmental change in arid Central Asia: impacts, vulnerability, and adaptations, J. Arid Environ., 73, 963–977, 2009. 5437, 5454
Mölg, T., Maussion, F., Yang, W., and Scherer, D.: The footprint of Asian monsoon dynamics in the mass and energy balance of a Tibetan glacier, The Cryosphere, 6, 1445–1461, doi:10.5194/tc-6-1445-2012, 2012. 5456
Mushkin, A. and Gillespie, A.: Using ASTER stereo images to quantify surface roughness, in: Land Remote Sensing and Global Environmental Change, Springer, Springer New York, 463–481, 2011. 5444
Mushkin, A., Gillespie, A., Danilina, I., O'Neal, M., Pietro, L., Abbott, E., and Balick, L.: Using sub-pixel roughness estimates from ASTER stereo images to compensate for roughness effects in the thermal infrared, in: RAQRS II: 2nd International Symposium on Recent Advances in Quantitative Remote Sensing, 25–29 September, Torrent, Valencia, 2006. 5444
Narama, C., Shimamura, Y., Nakayama, D., and Abdrakhmatov, K.: Recent changes of glacier coverage in the western Terskey-Alatoo range, Kyrgyz Republic, using Corona and Landsat, Ann. Glaciol., 43, 223–229, 2006. 5437
Narama, C., Kääb, A., Duishonakunov, M., and Abdrakhmatov, K.: Spatial variability of recent glacier area changes in the Tien Shan Mountains, Central Asia, using Corona (~1970), Landsat (~2000), and ALOS (~2007) satellite data, Global Planet. Change, 71, 42–54, 2010. 5437, 5451, 5453
Nie, Y., Liu, Q., and Liu, S.: Glacial lake expansion in the Central Himalayas by Landsat images, 1990–2010, PloS one, 8, e83973, doi:10.1371/journal.pone.0083973, 2013. 5441
Oerlemans, J.: Extracting a climate signal from 169 glacier records, Science, 308, 675–677, 2005. 5435
Osmonov, A., Bolch, T., Xi, C., Kurban, A., and Guo, W.: Glacier characteristics and changes in the Sary-Jaz River Basin (Central Tien Shan, Kyrgyzstan) 1990–2010, Remote Sens. Lett., 4, 725–734, 2013. 5437, 5440, 5451
Painter, T. H., Dozier, J., Roberts, D. A., Davis, R. E., and Green, R. O.: Retrieval of subpixel snow-covered area and grain size from imaging spectrometer data, Remote Sens. Environ., 85, 64–77, 2003. 5436

TCD
8, 5433–5483, 2014

Painter, T. H., Rittger, K., McKenzie, C., Slaughter, P., Davis, R. E., and Dozier, J.: Retrieval of subpixel snow covered area, grain size, and albedo from MODIS, Remote Sens. Environ., 113, 868–879, 2009. 5436

Palazzi, E., Hardenberg, J., and Provenzale, A.: Precipitation in the Hindu-Kush Karakoram Himalaya: observations and future scenarios, J. Geophys. Res.-Atmos., 118, 85–100, 2013. 5454, 5456

Paul, F.: Changes in glacier area in Tyrol, Austria, between 1969 and 1992 derived from Landsat 5 Thematic Mapper and Austrian Glacier Inventory data, Int. J. Remote Sens., 23, 787–799, 2002. 5435

Paul, F., Kaab, A., Maisch, M., Kellenberger, T., and Haeberli, W.: The new remote-sensing-derived Swiss glacier inventory: I. Methods, Ann. Glaciol., 34, 355–361, 2002. 5435, 5446

Paul, F., Huggel, C., and Kääb, A.: Combining satellite multispectral image data and a digital elevation model for mapping debris-covered glaciers, Remote Sens. Environ., 89, 510–518, 2004. 5435, 5436, 5441, 5442

Paul, F., Barrand, N., Baumann, S., Berthier, E., Bolch, T., Casey, K., Frey, H., Joshi, S., Konovalov, V., Bris, R. L., Mölg, N., Nosenko, G., Nuth, C., Pope, A., Racoviteanu, A., Rastner, P., Raup, B., Scharrer, K., Steffen, S., and Winsvold, S.: On the accuracy of glacier outlines derived from remote-sensing data, Ann. Glaciol., 54, 171–182, 2013. 5435, 5436, 5446, 5456

Pfeffer, W. T., Arendt, A., Bliss, A., Bolch, T., Cogley, J., Gardner, A., Hagen, J., Hock, R., Kaser, G., Kienholz, C., Miles, E., Moholdt, G., Mölg, Paul, F., Radić, V., Rastner, P., Raup, B., Rich, J., Sharp, M., and Consortium, T. R.: The Randolph Glacier Inventory: a globally complete inventory of glaciers, J. Glaciol., 60, 537–552, 2014. 5435, 5436, 5440

Quincey, D., Richardson, S., Luckman, A., Lucas, R., Reynolds, J., Hambrey, M., and Glasser, N.: Early recognition of glacial lake hazards in the Himalaya using remote sensing datasets, Global Planet. Change, 56, 137–152, 2007. 5441

Racoviteanu, A. E., Arnaud, Y., Williams, M. W., and Ordonez, J.: Decadal changes in glacier parameters in the Cordillera Blanca, Peru, derived from remote sensing, J. Glaciol., 54, 499–510, 2008a. 5435

Racoviteanu, A. E., Williams, M. W., and Barry, R. G.: Optical remote sensing of glacier characteristics: a review with focus on the Himalaya, Sensors, 8, 3355–3383, 2008b. 5435, 5436

Racoviteanu, A. E., Paul, F., Raup, B., Khalsa, S. J. S., and Armstrong, R.: Challenges and recommendations in mapping of glacier parameters from space: results of the 2008 Global Land

TCD
8, 5433–5483, 2014

Ice Measurements from Space (GLIMS) workshop, Boulder, Colorado, USA, Ann. Glaciol., 50, 53–69, 2009. 5435

Raup, B., Kääb, A., Kargel, J. S., Bishop, M. P., Hamilton, G., Lee, E., Paul, F., Rau, F., Soltesz, D., Khalsa, S. J. S., Beedle, M., and Helm, C.: Remote sensing and GIS technology in the Global Land Ice Measurements from Space (GLIMS) project, Comput. Geosci., 33, 104–125, 2007. 5435

Raup, B. H., Khalsa, S. J. S., Armstrong, R. L., Sneed, W. A., Hamilton, G. S., Paul, F., Cawkwell, F., Beedle, M. J., Menounos, B. P., Wheate, R. D., Shiyin, L., Xin, L., Donghui, S., Guodong, C., Kargel, J. S., Larsen, C. F., Molnia, B. F., Kincaid, J. L., Klein, A., and Konovalov, V.: Quality in the GLIMS glacier database, in: Global Land Ice Measurements from Space, Springer, Springer Berlin Heidelberg, 163–182, 2014. 5435, 5436

Ridley, J., Wiltshire, A., and Mathison, C.: More frequent occurrence of westerly disturbances in Karakoram up to 2100, Sci. Total Environ., 468, S31–S35, 2013. 5456

Saha, S., Moorthi, S., Pan, H.-L., Wu, X., Wang, J., Nadiga, S., Tripp, P., Kistler, R., Woollen, J., Behringer, D., Liu, H., Stokes, D., Grumbine, R., Gayno, G., Wang, J., Hou, Y.-T., Chuang, H.-Y., Juang, H.-M. H., Sela, J., Iredell, M., Treadon, R., Kleist, D., Van Delst, P., Keyser, D., Derber, J., Ek, M., Meng, J., Wei, H., Yang, R., Lord, S., Van Den Dool, H., Kumar, A., Wang, W., Long, C., Chelliah, M., Xue, Y., Huang, B., Schemm, J.-K., Ebisuzaki, W., Lin, R., Xie, P., Chen, M., Zhou, S., Higgins, W., Zou, C.-Z., Liu, Q., Chen, Y., Han, Y., Cucurull, L., Reynolds, R. W., Rutledge, G., and Goldberg, M.: The NCEP climate forecast system reanalysis., B. Am. Meteorol. Soc., 91, 2015–1057, doi:10.1175/2010BAMS3001.1 2010. 5439

Scherler, D., Bookhagen, B., and Strecker, M. R.: Spatially variable response of Himalayan glaciers to climate change affected by debris cover, Nat. Geosci., 4, 156–159, 2011a. 5436

Scherler, D., Bookhagen, B., and Strecker, M. R.: Hillslope-glacier coupling: the interplay of topography and glacial dynamics in High Asia, J. Geophys. Res.-Earth, 116, F02019, doi:10.1029/2010JF001751, 2011b. 5443

Schöne, T., Zech, C., Unger-Shayesteh, K., Rudenko, V., Thoss, H., Wetzel, H.-U., Gafurov, A., Illigner, J., and Zubovich, A.: A new permanent multi-parameter monitoring network in Central Asian high mountains–from measurements to data bases, Geosci. Instrum. Methods Data Syst., 2, 97–111, 2013. 5440

Shangguan, D., Liu, S., Ding, Y., Ding, L., Xu, J., and Jing, L.: Glacier changes during the last forty years in the Tarim Interior River basin, northwest China, Prog. Nat. Sci., 19, 727–732, 2009. 5437

TCD
8, 5433–5483, 2014

Sorg, A., Bolch, T., Stoffel, M., Solomina, O., and Beniston, M.: Climate change impacts on glaciers and runoff in Tien Shan (Central Asia), Nat. Clim. Change, 2, 725–731, 2012. 5437, 5455

Tedesco, M. and Narvekar, P. S.: Assessment of the NASA AMSR-E SWE product, selected topics in applied earth observations and remote sensing, IEEE J. Sel. Top. Appl., 3, 141–159, 2010. 5438

Tedesco, M., Kelly, R., Foster, J., and Chang, A.: AMSR-E/Aqua Daily L3 Global Snow Water Equivalent EASE-Grids V002, National Snow and Ice Data Center, Boulder, CO, 2004. 5438

Wan, Z.: New refinements and validation of the MODIS land-surface temperature/emissivity products, Remote Sens. Environ., 112, 59–74, 2008. 5439

Wang, K., Wan, Z., Wang, P., Sparrow, M., Liu, J., and Haginoya, S.: Evaluation and improvement of the MODIS land surface temperature/emissivity products using ground-based measurements at a semi-desert site on the western Tibetan Plateau, Int. J. Remote Sens., 28, 2549–2565, 2007. 5439

Worni, R., Huggel, C., and Stoffel, M.: Glacial lakes in the Indian Himalayas – from an area-wide glacial lake inventory to on-site and modeling based risk assessment of critical glacial lakes, Sci. Total Environ., 468, S71–S84, 2013. 5441

TCD
8, 5433–5483, 2014

Table 1. Data table listing Landsat scene IDs used in this study. Organized by WRS2 path/row combinations. Starred scene IDs denote "Master" images to which others were rectified.

	144/030	145/030	147/031
Number of Images	11	10	12
Date Range of Images	2002–2013		2000–2013
LT5 IDs	LT51440302006212IKR00	LT51450301998245BIK00*	LT51470312011231KHC01
	LT51440302009220KHC01	LT51450301998277BIK00	LT51470311998275BIK00
	LT51440301998270BIK00	LT51450302006203IKR00	LT51470312006249IKR00
	LT51440302011194IKR01	LT51450302007222IKR00	LT51470312007236IKR00
		LT51450302007254IKR00	LT51470312010276KHC00
		LT51450302009275KHC00	LT51470312011215KHC01
		LT51450302010214KHC00	
		LT51450302011185IKR00	
		LT51450302011249IKR01	
LE7 IDs	LE71440302002257SGS00*		LE71470312000257SGS00*
	LE71440302000188SGS01		LE71470312002278SGS00
	LE71440302000220SGS00		LE71470312002230SGS00
	LE71440302001158SGS00		
LC8 IDs	LC81440302013295LGN00	LC81450302013270LGN00	LC81470312013268LGN00
	LC81440302013231LGN00		LC81470312013252LGN00
	LC81440302013247LGN00		LC81470312014127LGN00
Projection	WGS 1984 45N		WGS 1984 44N
Comments	Eastern Edge of Study Area		Vicinity of Inylchek Glacier

	148/031	149/031	150/032
Number of Images	13	3	5
Date Range of Images	2002–2013	1999–2013	
LT5 IDs	LT51480312007259IKR00	LT51490312007250IKR00	LT51500321998296XXX00
	LT51480312011254IKR01		LT51500322009182KHC00
	LT51480311998234BIK00	LE71490311999252SGS00*	LE71500322001232SGS00*
	LT51480312006224IKR00		LE71500322002267SGS00
	LT51480312006256IKR00	LC81490312013282LGN00	LC81500322013161LGN00
	LT51480312007211IKR00	WGS 1984 43N	
LE7 IDs	LE71480312002205SGS00*		
	LE71480311999197EDC00		
	LE71480311999261SGS00		
	LE71480312002237SGS00		
LC8 IDs	LC81480312013211LGN00		
	LC81480312013275LGN00		
	LC81480312014134LGN00		
Projection	WGS 1984 44N		
Comments			

TCD
8, 5433–5483, 2014

Table 1. Continued.

	151/033	153/033
Number of Images	5	3
Date Range of Images	1998–2013	1998–2013
LT5 IDs	LT51510331998271XXX01 LT51510332009253KHC00	LT51530331998269AAA01
LE7 IDs	LE71510332000237SGS00* LE71510332001271SGS00	LE71530332002272SGS00*
LC8 IDs	LC81510332013280LGN00	LC81530332013278LGN00
Projection	WGS 1984 43N	WGS 1984 42N
Comments		Towards Pamir Knot

TCD
8, 5433–5483, 2014

Table 2. Data table comparing findings of previous glacial studies in the study region to the current study.

Author	Comparison Area	Published Changes	Published Period	Current Study	Period
Aizen et al. (2006)	Ashiirak Massif	−8.70 %	1977–2003	−3.4 ± 2 %	2003–2013
Narama et al. (2006)	Terskey-Alatoo	−8.00 %	1971–2002	−1.8 ± 2 %	2007–2013
Shannguan et al. (2009)	Central Tien Shan	−1.30 %	1965–2000	−1.7 ± 2 %	2000–2011
Osmonov et al. (2013)	Sary-Jaz River Basin	−3.70 ± 2.7 %	1990–2010	−1.5 ± 2 %	1999–2013

TCD
8, 5433–5483, 2014

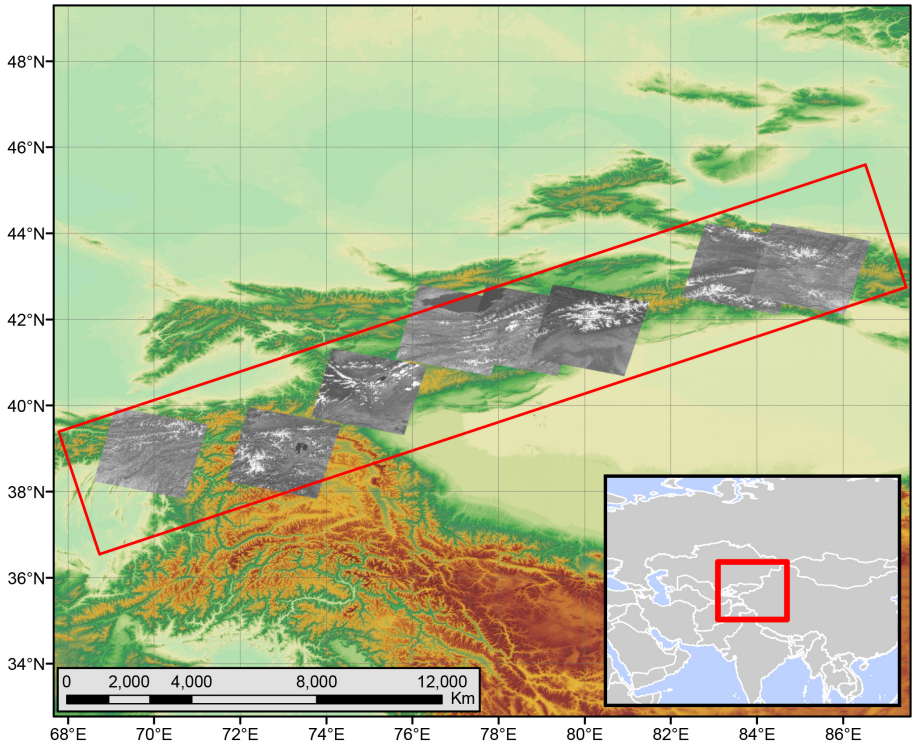

Figure 1. Study Area, showing SRTM V4.1 topography (Farr and Kobrick, 2000), locations of eight Landsat scenes outlines (grayscale) used in the study, and along-strike profile shown in Fig. 13 (red box).

TCD
8, 5433–5483, 2014

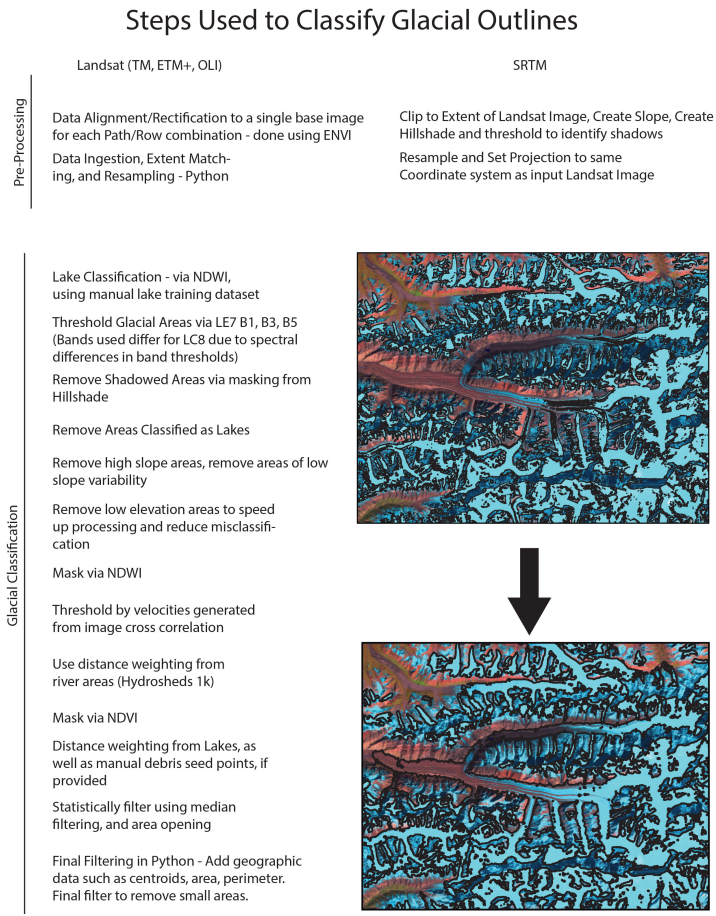

Figure 2. Steps of the algorithm as developed in this research, showing initial spectral classification vs final automated classification results on top of Landsat bands B7/B4/B2 loaded as red/green/blue, from image LE71470312000257SGS00.

TCD
8, 5433–5483, 2014

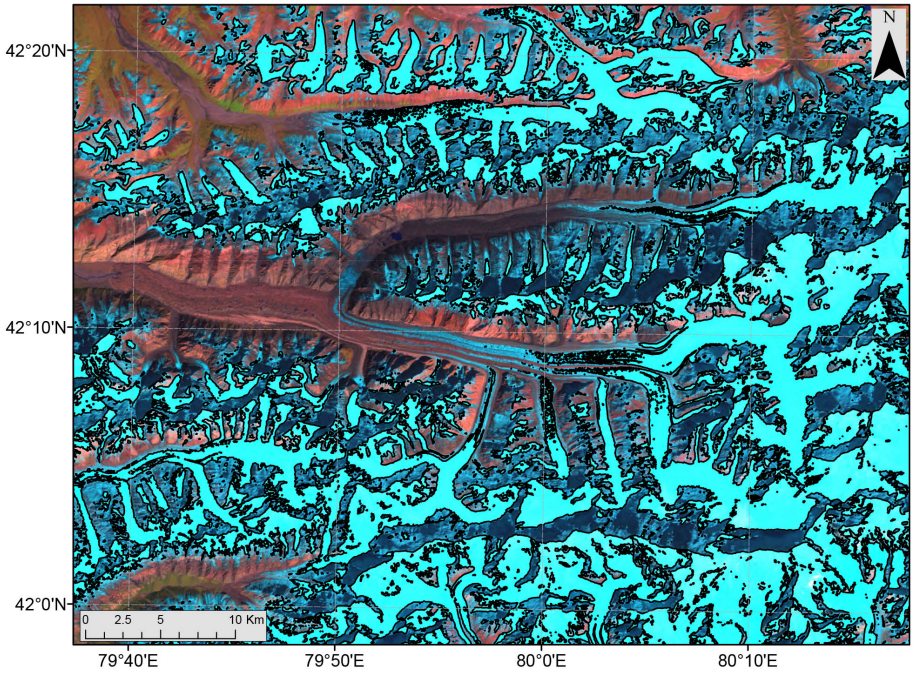

Figure 3. Spectrally delineated glacier outlines (Black), over Landsat bands B7/B4/B2 loaded as red/green/blue, from image LE71470312000257SGS00. Low reflectance on B7 (typical of glacial ice) results in glaciers being displayed as cyan.

TCD
8, 5433–5483, 2014

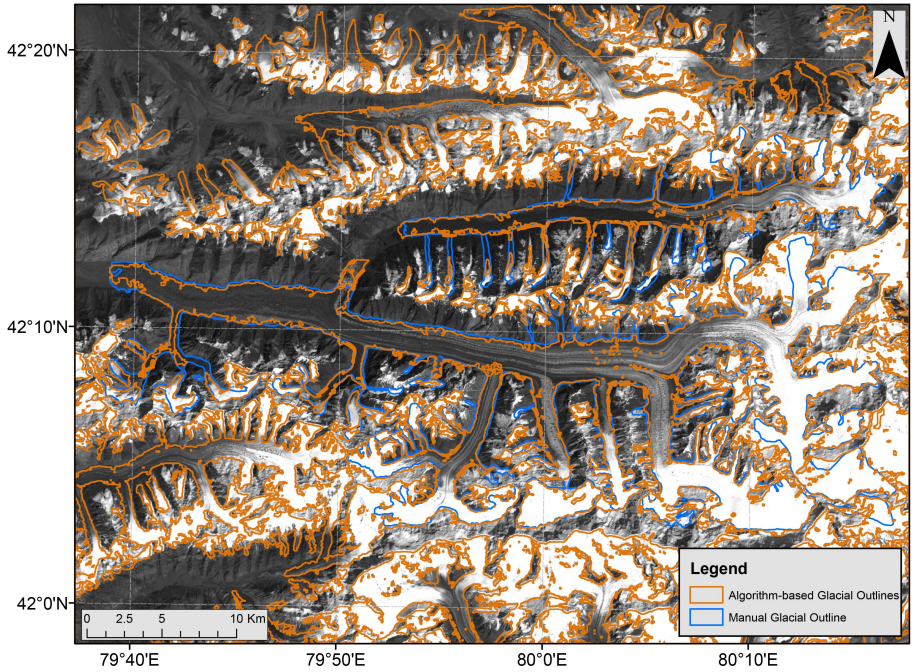

Figure 4. Manual glacier outlines (blue) and Algorithm outlines (with velocity and statistical filtering) (orange). Landsat band 8 in the background.

TCD
8, 5433–5483, 2014

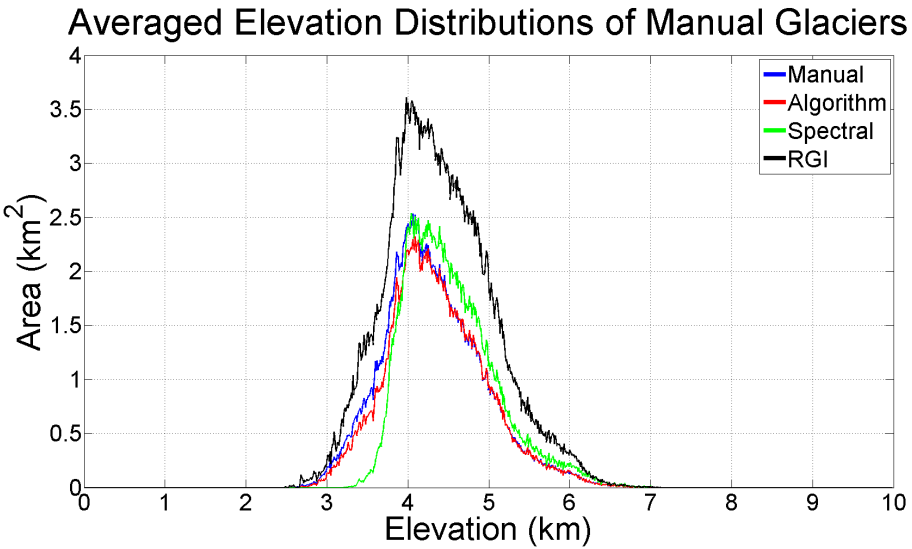

Figure 5. Bulk elevation distributions of sampled glaciers, with manual delineation (reference dataset, $n = 138$) in blue, algorithm-derived delineation in red, spectral delineation in green, and RGI in black.

TCD
8, 5433–5483, 2014

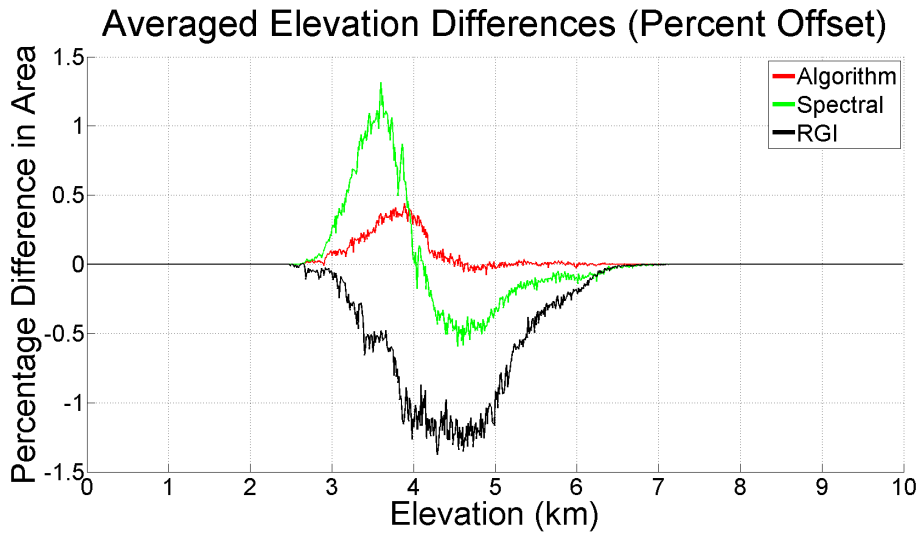

Figure 6. Percentage offset of area across elevation slices from a manual control dataset (n = 138), with algorithm-derived delineation in red, spectral delineation in green, and RGI in black.

TCD
8, 5433–5483, 2014

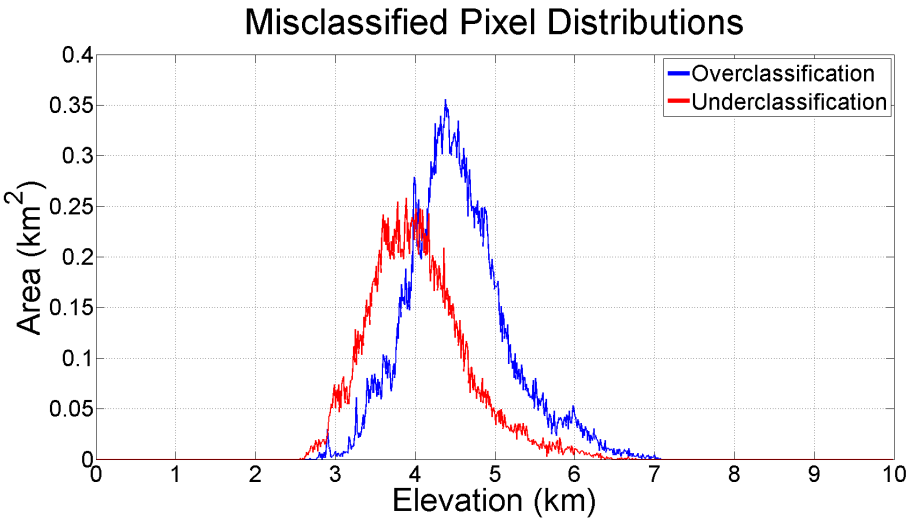

Figure 7. Elevation distributions of over- and under-classified glacial areas, as compared to a manual control dataset (n = 138).

TCD
8, 5433–5483, 2014

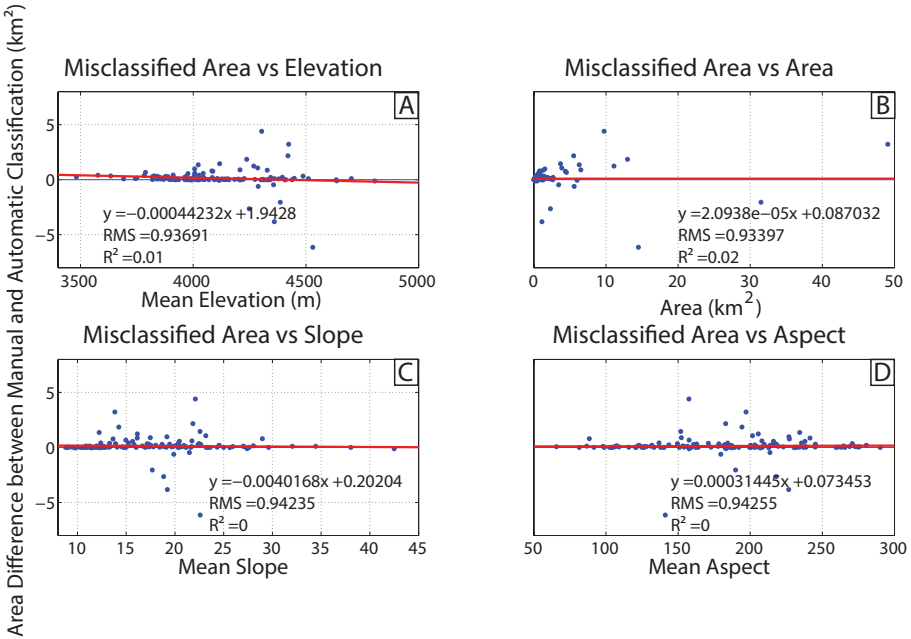

Figure 8. (a) Area mismatch vs average elevation of each glacier, **(b)** area mismatch vs area of glaciers, **(c)** area mismatch vs average slope, **(d)** area mismatch vs average aspect.

TCD
8, 5433–5483, 2014

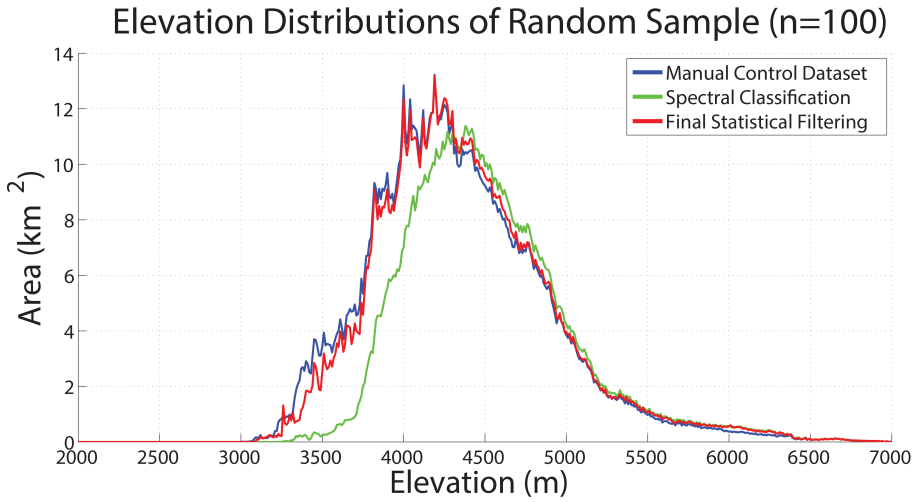

Figure 9. Averaged elevation differences for a random sample of glaciers overlapping a manual control dataset (n = 100).

TCD
8, 5433–5483, 2014

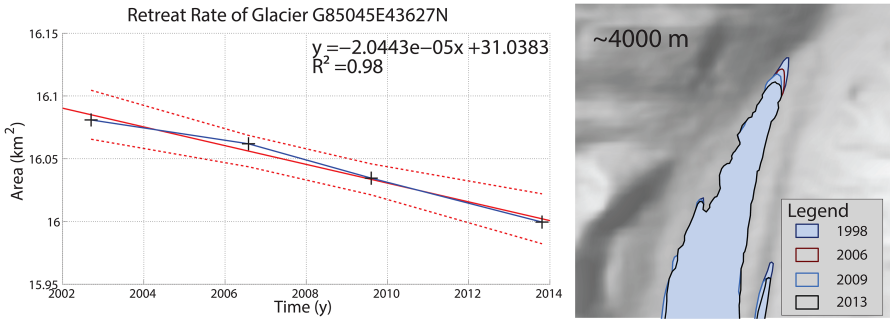

Figure 10. Area loss in a glacier towards the far east of the study area (85.045° E, 43.627° N), with 95 % confidence bounds. Loss: 0.5 ± 2 %, median glacial elevation 4000 m.

TCD
8, 5433–5483, 2014

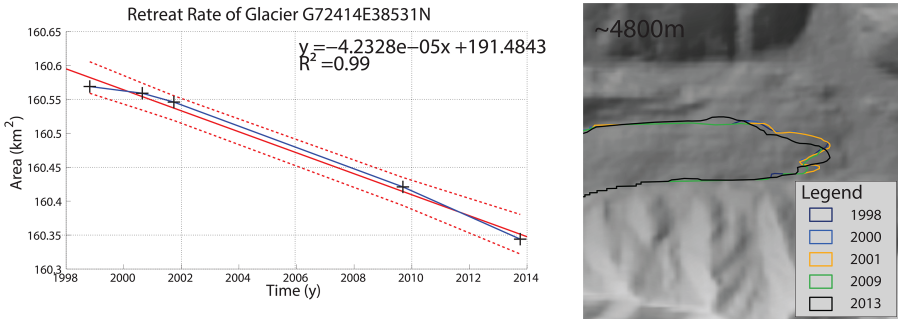

Figure 11. Area loss in a glacier towards the far west of the study area (72.414° E, 38.531° N), with 95 % confidence bounds. Loss: 0.1 ± 2 %, median glacial elevation 4800 m.

TCD
8, 5433–5483, 2014

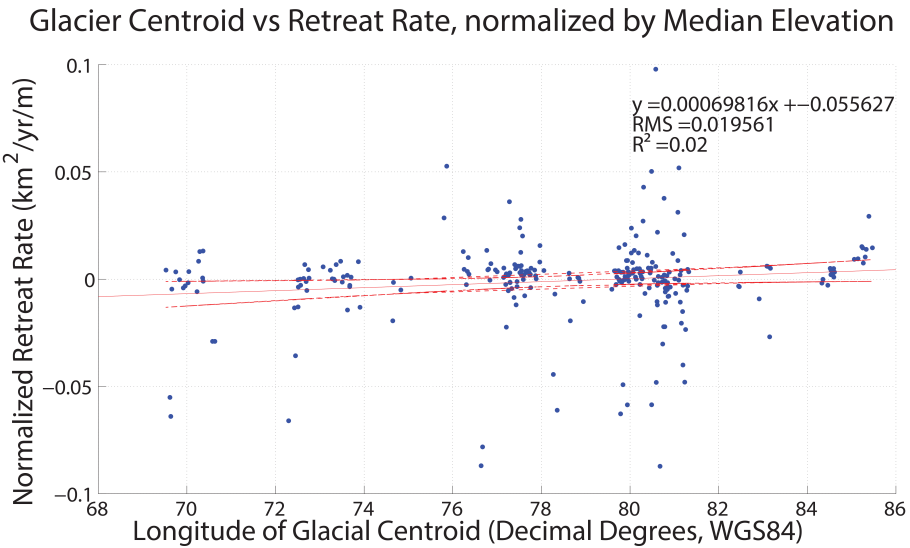

Figure 12. Area loss rates of index glaciers across the Tien Shan, showing a slight trend from west to east, with 95 % confidence bounds.

TCD
8, 5433–5483, 2014

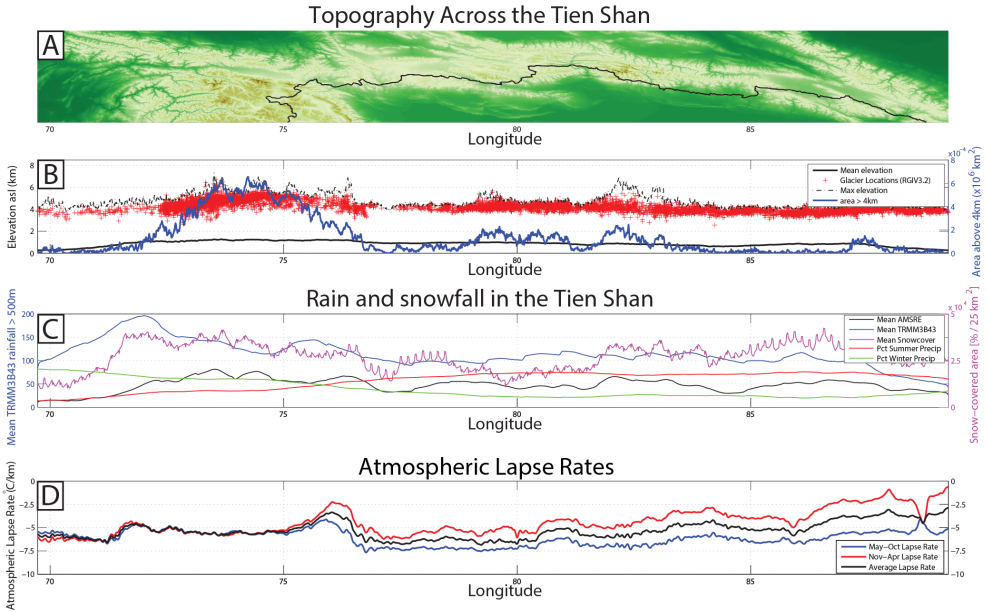

Figure 13. Swath Profile along the Tien Shan (swath outline presented in Fig. 1). **(a)** Topography of the swath profile, and generalized internal vs. external watershed delineation. **(b)** Mean and maximum elevation, as well as area above 4000 m. Glacier centroids and median elevations plotted in red. **(c)** SWE, TRMM precipitation data, and snow-covered area. Percentage of summer (red) and winter (green) precipitation from TRMM (1998–2013), on a scale of 0–100. **(d)** Atmospheric lapse rates. Average in black, November–April in red, May–October in blue.

TCD
8, 5433–5483, 2014

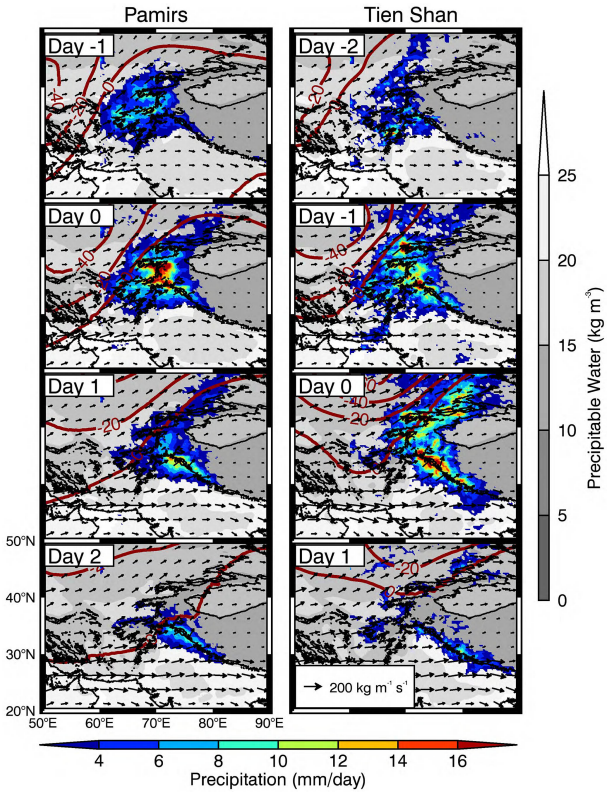

Figure 14. Lag composites of January–March, 1998–2013 extreme (95th percentile) precipitation events in the Pamirs (left) and Tien Shan (right). Color shows precipitation. Grayscale indicates column integrated precipitable water. Red contours indicate 500 hPa geopotential height anomalies. Vectors show vertically integrated moisture flux. Thick black contour indicates 2000 m topography contour. Data sources: TRMM 3B42 V7 and CFSR.

TCD
8, 5433–5483, 2014